communications earth & environment

Article

A Nature Portfolio journal

https://doi.org/10.1038/s43247-026-03300-w

Elevated ilmenite in lunar nearside cumulates revealed by extremely high-Ti glass beads augmented large-scale volcanism

Ziqing Li[1], Bo Zhang[1] ✉, Yuqi Qian[2] ✉, James W. Head[3], Tao Long[4] & Xiaochao Che[4]

The cause of mare asymmetry between the lunar nearside and farside remains a long-lasting conundrum. Due to scarcity of directly sourced deep samples, the formation mechanism of this phenomenon has not been well constrained. Here we characterized a class of rare impact glass beads with extremely high TiO_2 (16–25 wt%) and FeO (25–35 wt%) in the Chang'e-5 regolith. Petrological modeling indicates that the precursor rock of these glass beads cannot be formed through normal magmatic evolution, but rather has a deeper mantle origin. Phase diagram calculations show that the precursor rock has a typical mineral assemblage similar to ilmenite-bearing cumulates. Based on different residual anorthite proportions, the restored Lunar Magma Ocean (LMO) original crystalline mineral assemblage is predicted to contain ~15–20 vol% ilmenite, significantly higher than the average predicted levels. Therefore, the nearside ilmenite-bearing cumulates may have higher ilmenite abundance than farside, causing increased partial melting and more abundant volcanism.

The origin of the asymmetry between the nearside and the farside of the Moon remains a long-term unresolved issue, represented by dichotomies in crustal thickness[1], topography[2], basalt distribution[3,4], and thorium (Th) concentration distribution[3]. The vast majority of mare basalts are distributed on the nearside (~93%), especially in the Procellarum KREEP Terrane (PKT), and a very small amount is located near large impact basins on the farside[5,6], mainly in the South Pole-Aitken (SPA) basin[7]. A series of studies have attributed the larger basalt area and volumes on the nearside to a thinner anorthositic crust than the farside[8,9], which favors nearside magma ascent and eruptions[10]. However, the lack of abundant mare basalts in the South Pole-Aitken basin on the farside with thin crust (<30 km) indicates that crustal thickness might not be the only factor controlling basalt eruptions[9–12] in the SPA basin (e.g., the removal of megaregolith by the SPA impact could have facilitate the mantle cooling and limited the magma generation in the area)[11]. Based on the analysis of Apollo and meteorite samples[13,14] as well as numerical simulations[15], an alternative hypothesis suggests that the dichotomy of mare basalt abundance may be controlled by the heterogeneity of the highly fractionated product (ur)KREEP and/or ilmenite-bearing cumulate (IBC). The (ur)KREEP was the late residue of lunar magma ocean (LMO) solidification enriched in potassium (K), rare earth elements (REE), and phosphorus (P)[13,16,17]. Therefore, this reservoir can undergo enhanced radioactive decay heating, prolonging the duration and expanding the extent of volcanic activity on the nearside[15]. However, this speculation has been challenged by the recently returned Chang'e-5 samples, as isotopic evidence indicates that these young mare basalts (2.0 Ga)[18,19] were minimally affected by elevated KREEP abundances in their mantle source regions[20,21]. Alternatively, these basalts could have been formed by merely indirect heating from the subcrustal KREEP layer[22]. Similarly, the young Chang'e-6 basalts of ~2.8 Ga[23–25] returned from lunar farside were also considered to originate from a depleted mantle source based on Sr-Nd isotopic evidence[26], suggesting a volcanism lacking KREEP components in the SPA basin. In contrast, the extensive overturning of the IBC layer, concentrated on the nearside, is considered an effective way to reduce the melting point and increase the melting degree of the lunar mantle, especially in the young Chang'e-5 basalts[27,28], thereby facilitating possibly long-lasting and large-scale nearside volcanism. This melting mechanism is also supported by geodynamic simulations[29] and aligns with remote sensing observations[30,31]. Nonetheless, the knowledge of the different

[1]State Key Laboratory of Deep Earth and Mineral Exploration, School of Earth and Space Sciences, Peking University, Beijing, China. [2]NWU-HKU Joint Center of Earth and Planetary Sciences & Department of Earth and Planetary Sciences, The University of Hong Kong, Hong Kong, China. [3]Department of Earth, Environmental, and Planetary Sciences, Brown University, Providence, RI, USA. [4]The Beijing SHRIMP Center, Institute of Geology, Chinese Academy of Geological Sciences, Beijing, China. ✉e-mail: geozhangbo@pku.edu.cn; yuqiqian@hku.hk

evolutionary processes of mare basalts on these two opposite hemispheres caused by this compositional heterogeneity is still limited due to the scarcity of direct deep mantle samples.

Recently, China's Chang'e-5 mission successfully returned regolith samples[32] from the northwestern part of Procellarum KREEP Terrane[33], which provides a unique opportunity to explore volcanic process in this distinctive geochemical province. The regolith is mainly composed of local basaltic components, but also involves the addition of <10% exotic materials[34,35]. These exotic components include materials originating from the lunar mantle, such as primitive Mg-suite melts[36] and ultramafic cumulate glass[37]. These samples, originating in the deep mantle, provide direct information for the formation and evolution of the Moon.

In this study, we characterize a class of extremely high-Ti glass beads (16–25 wt%) in the Chang'e-5 regolith sample. Based on geochemical analysis and petrological modeling, the precursor rock of these high-Ti glass beads may have originated from ilmenite-bearing cumulates beneath the PKT. These nearside samples have significantly higher ilmenite abundance (15–20 vol%) than the average level (less than 10 vol%), which increases the degree of lunar mantle melting and the scale of volcanic activity in the PKT.

Results

We extracted four glass beads from the powder sample CE5C0600, allocated by the China National Space Administration (CNSA). These glass beads are characterized by approximate spherical or ellipsoidal shapes with grain size ranging from 50 to 150 μm (Fig. 1). The interior of these glass beads is generally heterogeneous. Specifically, samples G107 and G114 mainly contain circular nanoscale metallic iron particles (Fig. 1A, C), which are considered as typical impact-derived products from thermal decomposition[38,39] or liquid immiscibility processes[40,41]. While samples G108 and G230 contain more mineral fragments and a large number of vesicles inside the amorphous matrix (Fig. 1B, D), which may originate from incomplete melting caused by instantaneous impact[42,43].

The major element compositions of these glass beads were measured by an electron microprobe analyzer (Supplementary Data 1). To ensure the statistical significance of the data and understand the heterogeneity of the samples, 17–20 point analyses (Supplementary Data 1) and Ti element mapping were performed on each sample (Supplementary Fig. 1). The mapping results show that these glass beads are not homogeneous, with significant changes in the Ti element (Supplementary Fig. 1A–C). In contrast, the quantitative analysis of clean areas indicates the composition variation of the matrix is limited, and the variation range of TiO_2 content is only within ~2.5 wt% (Supplementary Fig. 1). In order to improve the database of the study, we incorporated three similar glass beads from ref. 44 to the current study. These seven glass beads were collected from the same sampling site and have similar compositions especially their high-Ti features (Supplementary Data 1), which may represent a class of glass beads with the same origin (Fig. 2). These seven glass beads present low SiO_2 (24.63–32.16 wt%), Al_2O_3 (4.34–8.67 wt%), CaO (5.57–8.48 wt%), MgO (3.35–5.96 wt%), high FeO (25.91–34.90 wt%) and extremely high TiO_2 (16.61–24.91 wt%) (Fig. 2A–E and Supplementary Data 1). The impact

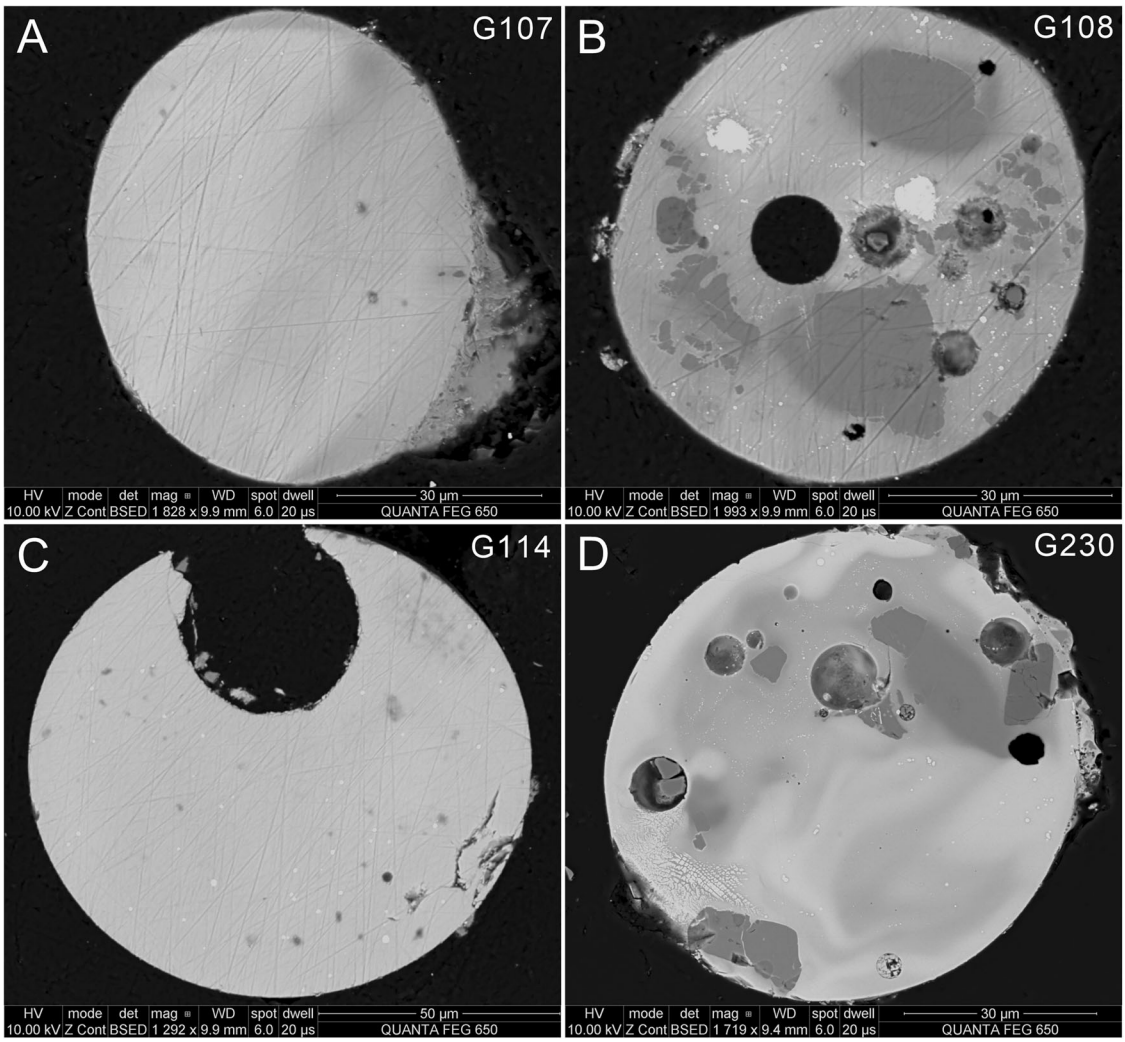

Fig. 1 | Microstructures of high-Ti glass beads from Chang'e-5 regolith CE5C0600. A Glass bead G107. **B** Glass bead G108. **C** Glass bead G114. **D** Glass bead G230.

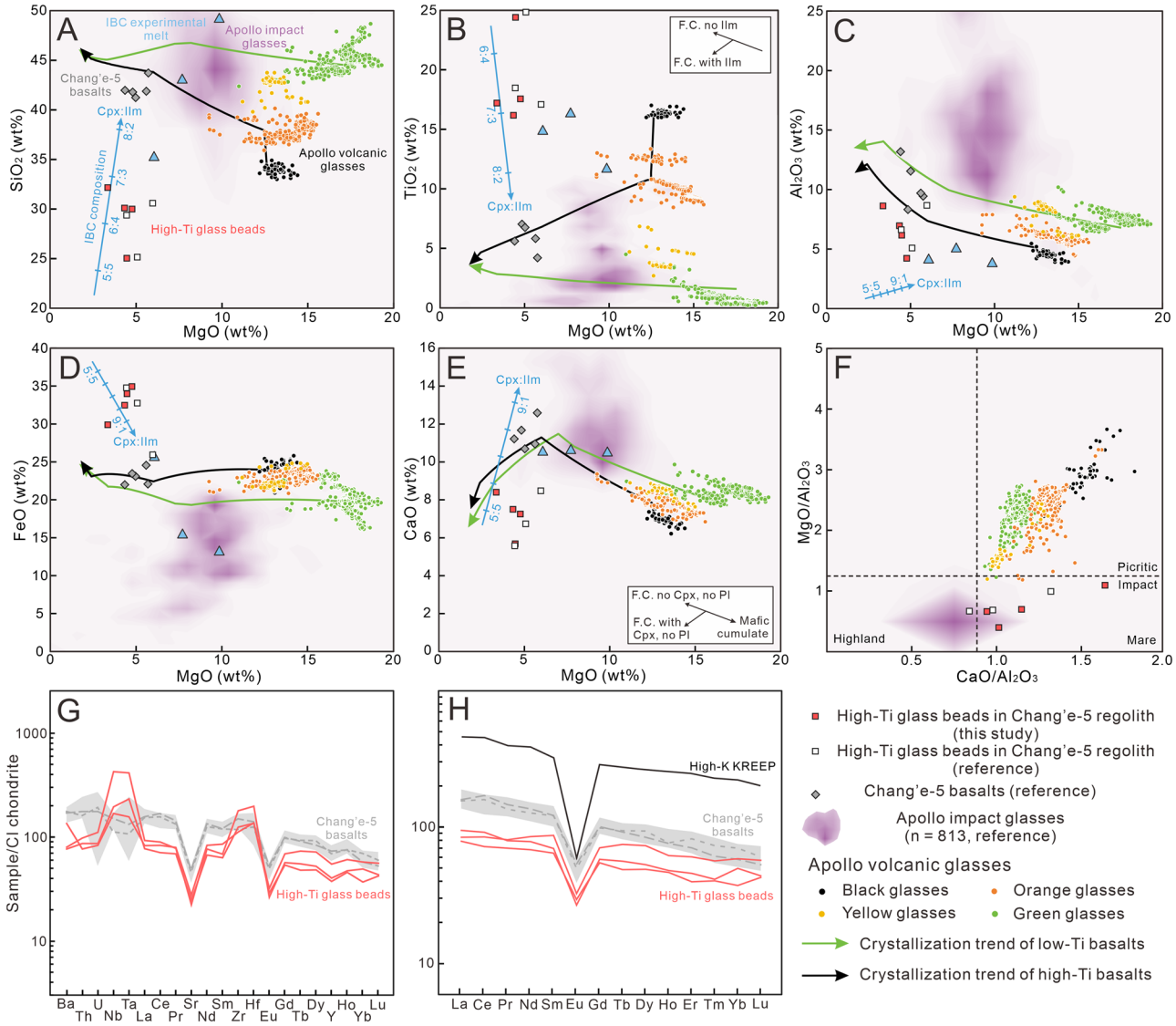

Fig. 2 | Geochemical characteristics of high-Ti glass beads. **A** MgO versus SiO_2. **B** MgO versus TiO_2. **C** MgO versus Al_2O_3. **D** MgO versus FeO. **E** MgO versus CaO. Three high-Ti glass beads are from ref. 44. Apollo volcanic glasses are from refs. 44,47,89,90. Apollo impact glasses are from refs. 91–100. Chang'e-5 basalt data are from refs. 18,20,27,101,102. The fractional crystallization trend was defined by ref. 27. The light blue triangle represents the melt composition formed by partial melting of IBC obtained from experimental petrology studies[55]. The blue line represents the changes in IBC composition caused by various proportions of Cpx and Ilm[56]. **F** CaO/Al_2O_3 ratio and MgO/Al_2O_3 ratio binary diagram distinguishing the volcanic versus impact origin of glass bead in the regolith samples[1]. **G** Chondrite-normalized trace element patterns from three analyses of the high-Ti glass beads (red solid line). **H** Chondrite-normalized REE patterns from three analyses of the high-Ti glass beads (red solid line). The gray area shows the range of the Chang'e-5 basalts[21]. Chondrite values are from ref. 103. High-K KREEP are from ref. 88. Ol olivine, Opx orthopyroxene, Cpx clinopyroxene, Pl plagioclase, Ilm ilmenite, FC fractional crystallization.

texture features such as nanophase iron and/or mineral fragments (Fig. 1) indicate that these samples were not typical volcanic origin[45,46] and the expected high MgO content typically found in volcanic glasses (the "picritic glasses"[45,47]) (Supplementary Data 2) was also not observed in these samples. Overall, these glass beads are more consistent with the characteristics of impact-generated glasses than with typical volcanic glasses based on their textures and chemical composition. Also, the compositional classification shows that these samples are located in the impact glass bead area and mare glass bead areas of the CaO/Al_2O_3-MgO/Al_2O_3 diagram[48] (Fig. 2F).

Considering that one of the glass beads was too small to place the test point of LA-ICP-MS, only three glass beads were measured for trace elements. The trace element results reveal significant enrichment of high field strength elements, including Nb (40.8–103.8 ppm), Ta (2.1–5.7 ppm), Zr (432.7–693.9 ppm), and Hf (14.2–20.6 ppm) (Fig. 2G). The overall rare earth element (REE) content is ~80–100 times higher than that of chondrite meteorite (Fig. 2H). The REE patterns show minor variability with light LREE enrichment and are characterized by pronounced negative Eu anomalies (δEu = 0.42–0.50) (Fig. 2H). The Ni and Co content in the glass beads are 44.5–80.8 ppm and 28.9–37.5 ppm, respectively, similar to the range of other impact glasses[44].

Discussion

Volcanic or impact glass beads?

Distinguishing the volcanic or impact origin of the high-Ti glass beads is critical for their interpretation. These high-Ti glass beads can be identified as typical impact glass beads rather than volcanic melt due to their impact textures and similar chemical compositions as reported impact glasses (Figs. 1 and 2). Based on these observations, these high-Ti glass beads in the Chang'e-5 regolith are interpreted to be of impact origin, formed by high-velocity impact events on the mare basalt protolith[49] and the regolith[50].

Possible precursor source of high-Ti glass beads

Lunar samples could exhibit high TiO_2 content, but these seven high-Ti glass beads exceed previously reported values, with TiO_2 content of 16.61–24.91 wt%. In this case, such extreme TiO_2 enrichment makes it crucial to determine whether these elevated contents were caused by impact processes, including elemental loss[42,51] and/or mineral heterogeneous distribution[52]. Compiled Chang'e-5 basalt and Chang'e-5 impact glass data show that most elements with low to moderate volatility, such as Ti and Al maintain similar contents to the source rock[42,43] (Supplementary Fig. 2 and Data 3). Even if there is a certain linear loss relationship, the maximum loss does not exceed 2 wt%[43] (Supplementary Fig. 2 and Data 3). These results indicate that the volatile loss process caused by impact cannot lead to significant enrichment of the Ti element. Therefore, the high TiO_2 contents of these glass beads cannot reasonably be explained by impact-related elemental modification. Alternatively, the increase of certain specific elements in small glass beads (<100 μm) may be attributed to the increase of mineral abundance (e.g., ilmenite) in the local basalt, caused by local small-scale impacts, as suggested by Wang et al. (2025)[52]. Specifically, small-scale impacts on areas with heterogeneous mineral distribution often result in a change in the content of certain characteristic elements (e.g., plagioclase-Al and ilmenite-Ti) in the product, and the formation of small-sized glass beads (<100 μm). In fact, three glass beads in this study could match with this size range but one exception is that glass bead G114 falls outside this range, so it cannot be explained by this mechanism. In addition, we conducted principal component analysis (PCA, a multivariate projection that summarizes covariation among major elements) on the high-Ti glass beads in this study and Chang'e-5 impact glass beads based on the methods from a previous study[52] (Supplementary Fig. 3). As suggested by ref. 52, the PCA analysis could be applied on evaluating the elements variation with different mineral abundances (e.g., plagioclase-Al and ilmenite-Ti) and distinguishing the element clustering with host-basalt compositions[52]. The results show that the high-Ti glass beads in this study deviated significantly from the trend of increasing Ti element in the Chang'e-5 local impact glass beads caused by rising ilmenite abundance (Supplementary Fig. 3). This indicates that the formation of these samples could not be attributed to the variation in the ilmenite abundance of Chang'e-5 local basalt, but rather to their distinct exotic origin. Therefore, the composition of these high-Ti glass beads largely represents the inherent characteristics (especially the unique high TiO_2 features) of their precursor rock rather than modification from impact processes, and the possible precursor rock source can be identified through these major elements.

After excluding the impact effect, the high-Ti precursor rocks of these glass beads were most likely formed through magmatic processes, especially fractional crystallization and associated cumulate formation. In fact, it is possible for fractional crystallization and cumulate production[10,53] to have occurred in the thick lava layer (~50 m) at the Chang'e-5 sampling site. Therefore, we calculated the mineral abundance and composition of the cumulate produced by the fractional crystallization of Chang'e-5 lava flows (Supplementary Fig. 4 and Data 4). The results show that the cumulate is mainly composed of over 50% clinopyroxene with less than 10% ilmenite (Supplementary Fig. 4 and Data 4), therefore, it cannot be a candidate origin for the precursor rocks. Furthermore, we selected compositions of high-Ti (black glasses) endmembers as a high-Ti basalt source region for fractional crystallization modeling (Fig. 2A–E and Supplementary Data 5) and combined the results with previous modeling of low-Ti basalts[27] to comprehensively extend this assessment to the currently available lunar samples. In fact, the evolutionary region of these two endmembers covers the majority of mare basalt compositions, but still cannot match the sample composition in this study, especially for their low SiO_2, high TiO_2 and FeO characteristics (Fig. 2A, B, D). In summary, the precursor rock of these high-Ti glass beads may not have originated from normal magma evolution processes. In this case, a potential high-Ti source consistent with the features of these samples may be IBC in the lunar mantle and its derived melts, as indicated by numerous petrological experiments[54–56].

To constrain the melting behavior, mineral abundance, and composition of possible precursor rock corresponding to the bulk chemical composition of the high-Ti glass beads, we undertook phase equilibrium modeling and pseudosection calculations (Fig. 3). We calculated a P-T diagram for 1000 °C to 1400 °C and 1 to 4 kbar based on the measured average bulk composition of seven high-Ti glass beads (Supplementary Data 1) with the maximum P (4 kbar) corresponding to a depth of around 75 km, encompassing the lunar crust and uppermost mantle[17]. Based on the P-T phase diagram, the solidus line of these high-Ti glasses is approximately 1070 °C and does not change significantly with pressure, while the liquidus line exceeds 1400 °C (Fig. 3A). During the process of equilibrium cooling to below 1070 °C, the melt can be completely restored to the composition of the solid precursor rock. The mineral assemblage in the precursor rock of all high-Ti glass beads mainly includes clinopyroxene, ilmenite, anorthite, olivine and spinel (Fig. 3A). Considering the potential influence of slight differences in the bulk composition, we calculated the mineral modal abundance and mineral composition of the precursor rock for each of the seven samples, respectively (Fig. 3B and Supplementary Data 6). The calculated results show that the modal proportion range of clinopyroxene, ilmenite, anorthite and olivine are, respectively, 29.0–47.0 vol%, 24.1–37.7 vol%, 12.7–29.3 vol%, and 1.2–21.7 vol%. The modal abundance of spinel has not been shown as it is generally less than 1 vol% (Supplementary Data 6). The clinopyroxene has a composition of $En_{21.1\text{-}36.2}Fs_{39.6\text{-}60.9}Wo_{12.9\text{-}29.8}$, and olivine is fayalite with a composition $Fo_{15.6\text{-}33.7}$ (Fig. 3C, D). These calculations indicate that the precursor rock of the high-Ti glass beads has extremely high ilmenite abundance, which is also supported by the observed enrichment of high field strength elements (Fig. 2G) as they tend to enter into ilmenite crystals[57,58].

Based on remote sensing observations, we explored potential candidate terrains on the lunar surface for this unique precursor rock. This type of rock, with such high ilmenite abundance (high-Ti, 15–25 wt%), seems to be rare on the lunar surface. The LROC WAC TiO_2 content map showed that the northwestern portion of Mare Tranquillitatis indeed has the highest TiO_2 content on the entire Moon with a refined value of ~12.6 wt%[30]. In this case, existing lunar surface rock units appear not matching with the high-Ti glass beads in this study due to their low TiO_2 content. Therefore, we conclude that the precursor rock of the Chang'e-5 high-Ti glass beads that we analyzed were excavated and originated from deep layer beneath the regolith.

As suggested by numerous petrological experiments and theoretical calculations[59–62], the initial lunar magma ocean (LMO) crystallization will form early ultramafic cumulates (mainly olivine + orthopyroxene) and late ilmenite-bearing cumulates (IBC, mainly clinopyroxene + ilmenite). Many petrological experiments indicate that IBC and its related derived melts could produce materials with sufficiently high TiO_2 content, which could be considered as a potential source for high-Ti precursor rock in this study. The hybridization experiments between early cumulate and IBC have shown that the source region of Apollo volcanic high-Ti glass beads can be formed by introducing late IBC into the deep mantle through the mantle overturn[54,55]. However, this mixing process with early high-Mg cumulate will lead to the formation of picritic melt[54], which is inconsistent with the high-Ti glass beads with low MgO content (MgO <5 wt%) in this study. In contrast, independent partial melting of late-stage low-Mg IBC tends to produce the Mg-poor magma but the maximum TiO_2 and FeO content in the IBC melt can only reach ~16 wt% and ~25 wt% based on petrological experiments[55] (Fig. 2), which cannot match with samples in this study. Alternatively, these high-Ti glass beads are originated directly from IBC itself rather than derived melt. The consistency between the mineral composition and the LMO crystallization trend defined by petrological experiments[61] also supports that hypothesis that this precursor rock may be a late-stage product of LMO crystallization (Fig. 3C, D). The clinopyroxene/ilmenite ratio of precursor rock in this study is ~0.87–1.49, which is consistent with IBC bulk mineralogy (clinopyroxene/ilmenite ratio = ~1.0) required to forms high-Ti basalt suggested by previous experiment[56]. Our REE modeling also indicates that 10–50% KREEP contamination can

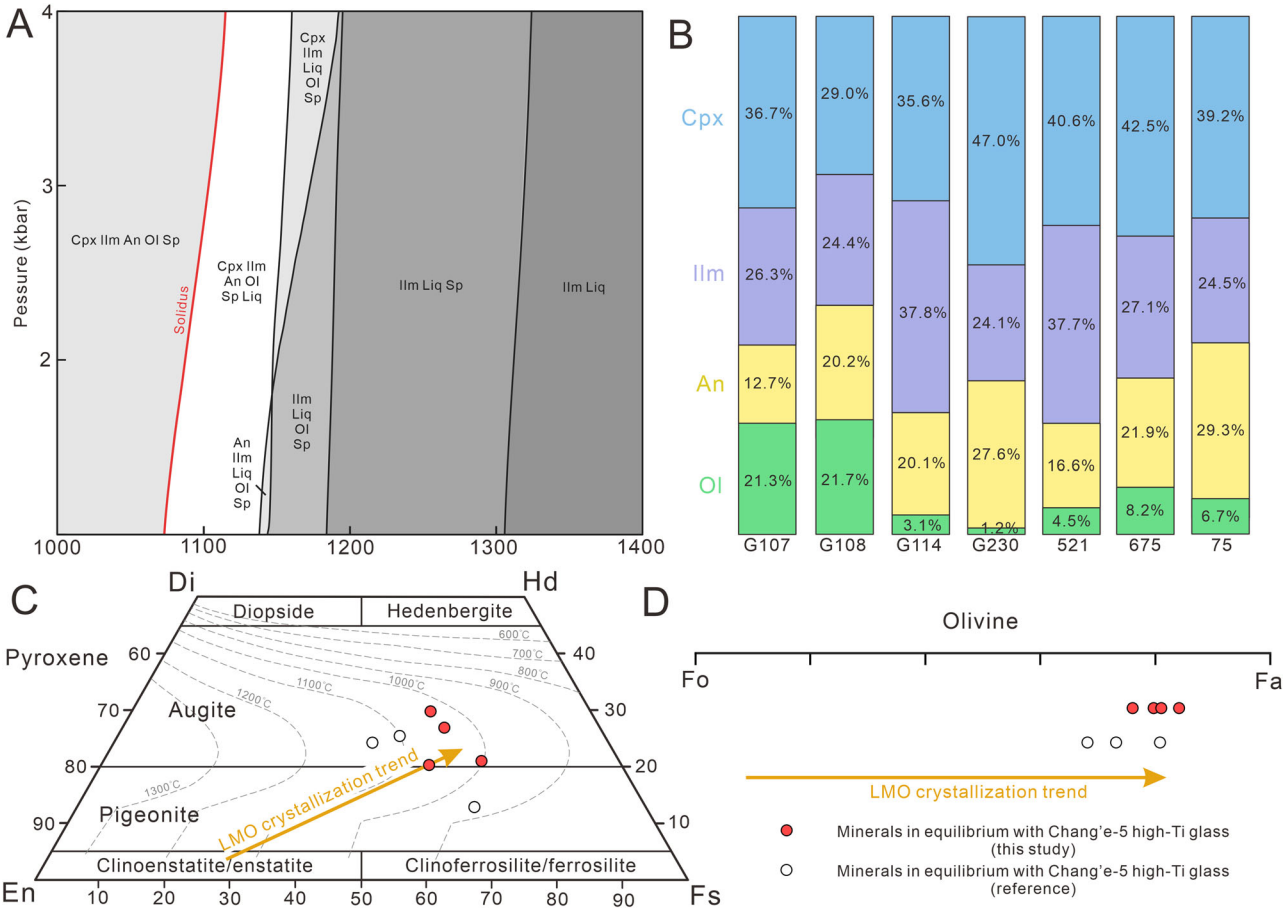

Fig. 3 | Model mineral components and composition of the equilibrium phases corresponding to the composition of high-Ti glass beads. A Phase diagram based on average composition of high-Ti glass beads. **B** The mineral modal abundance in the precursor rock of each glass bead. **C**, **D** Pyroxene and olivine compositions in equilibrium phases. The LMO crystallization trend was defined by ref. 61. Liq liquid, Sp spinel, Ol olivine, Cpx clinopyroxene, An anorthite; Ilm ilmenite.

produce REE patterns consistent with those observed (Supplementary Fig. 5 and Data 7), supporting its interpretation as a late-stage cumulate. Therefore, the precursor rock of these high-Ti glass beads may represent primary ilmenite-bearing cumulate from late-stage LMO crystallization.

Elevated ilmenite abundance in the nearside IBC

Remote sensing observations and ejecta distribution modeling indicate that exotic materials in the surface regolith at the Chang'e-5 landing site are mainly from the lateral transport of surrounding impact crater ejects, such as Aristarchus or Copernicus craters[63,64]. Similarly, the analysis of exotic components in Chang'e-5 regolith samples indicates that other units in the PKT could be regarded as significant contributors of exotic materials[34]. In addition, considering that the lunar mantle materials likely require large (potentially basin-forming) events to bring them to the surface[65,66], the materials beneath the high-Ti units in the PKT can be considered as a potential source region of precursor rock in this study. For example, the precursor rock may have been excavated during the impact that formed the Imbrium basin and subsequently transported to the Chang'e-5 landing site.

If the precursor rock represents the shallow late-stage IBC cumulate composition below the PKT in the nearside, the local LMO crystallization process could be restored based on its composition. Considering that quartz and a portion of anorthite float to form the lunar crust[59], we restored the mineral modal abundance of LMO crystallization (that is, the mineral abundance before anorthite flotation) under different proportions of residual anorthite in the IBC (Fig. 4A, B and Supplementary Data 8). These calculations show that the total anorthite modal abundance crystallized from the LMO will exceed 50% when the residual anorthite is less than 15% (Fig. 4B, Supplementary Fig. 6, and Data 8), which tends to form a thicker lunar crust (beyond 50 km) exceeding the observed result (34–43 km)[67]. Within a reasonable floating efficiency of 70–80%[67], the estimated abundance of anorthite and olivine is highly consistent with the corresponding mineral ranges calculated in various LMO models and the clinopyroxene approximately matches the abundance within the error range albeit slightly lower (Fig. 4B). In contrast, the ilmenite modal abundance is 15–20%, significantly exceeding that in LMO modeling calculations under a global average magmatic ocean condition[59–62](Fig. 4B). From this perspective, the IBC composition obtained in this study appears to indicate a cumulate on the nearside that is richer in ilmenite than the average IBC.

To evaluate the influence of nearside IBC with higher ilmenite abundance on magma production, we conducted phase equilibrium calculations based on compositions of average IBC[59,68] and the IBC in this study (Fig. 4C and Supplementary Data 9). The calculated phase diagram at 3 kbar shows that the IBC with higher ilmenite abundance in this study depresses the solidus by ~80 °C compared to the average IBC (Fig. 4C). In addition, the 20–80 vol% melt isopleths form a diagonal band that shifts to lower temperature with increasing ilmenite content (Fig. 4C). Especially, the melt fraction increases from ~20–30 vol% at the average IBC end-member to ~60–70 vol% near the IBC in this study (Fig. 4C). This behavior indicates that IBC in this study not only begins to melt at lower temperatures, but also produces substantially higher melt volumes than the average IBC under the same thermal conditions. The pseudosection further reveals systematic changes in the residual mineral assemblage from Cpx + Ilm + Qtz at the average IBC end to Cpx + Ilm + An ± Ol for the IBC in this study, implying progressively more mafic residues. Such compositional and phase-equilibrium effects mean that nearside regions containing ilmenite-rich IBC are more prone to cross the solidus, reach higher degrees of partial

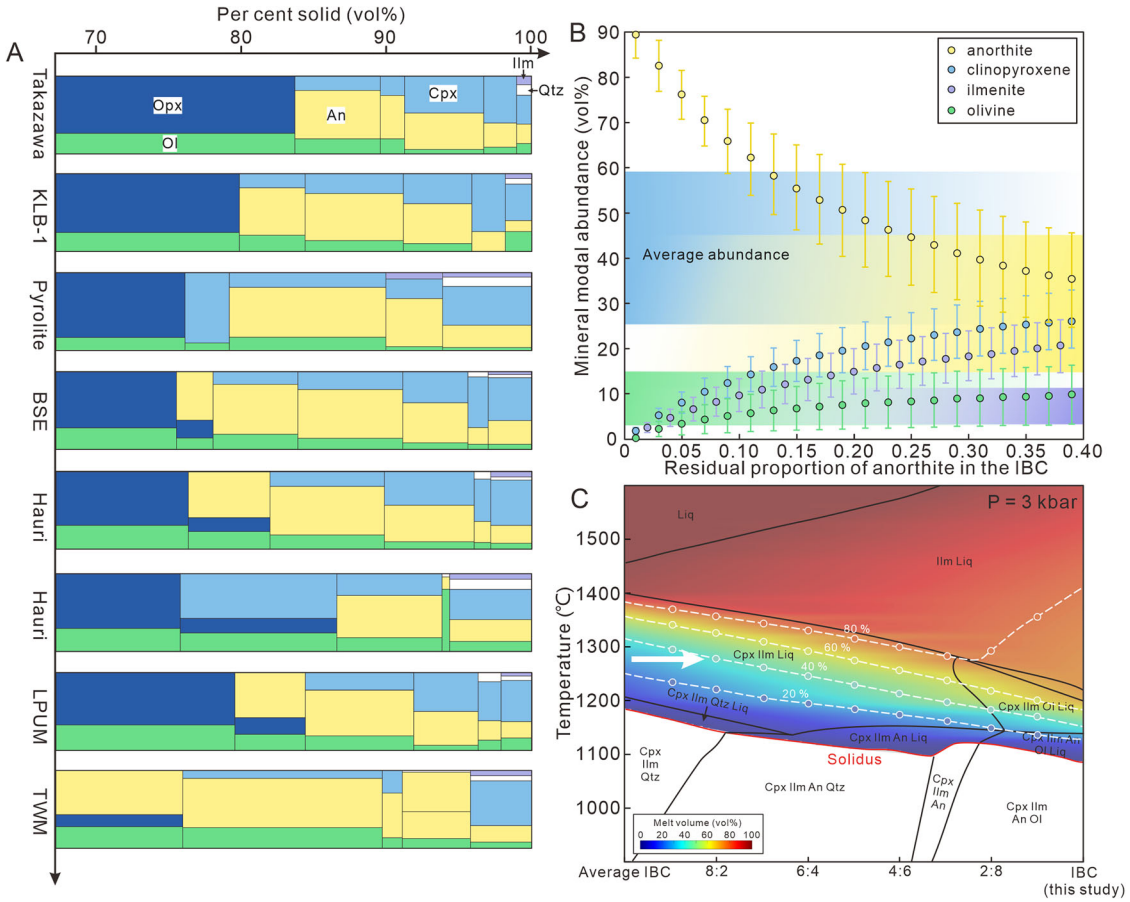

Fig. 4 | Calculation of LMO crystalline minerals. A Crystallization sequences of different LMO models by refs. 60,61,103–109. **B** Mineral assemblage in the LMO restored under different residual anorthite proportions. Solid dots represent the calculated values in this study and error bars in the same color show the range of mineral modal abundance in the calculations of this study, while the corresponding color regions represent the theoretical calculated full abundance variation range from minimum to maximum predicted by seven models presented in (**A**). **C** Phase diagram between average IBC and IBC composition in this study. The phase diagrams of the nearside IBC and the average IBC used the compositions from this study and the ref. 68, respectively. The average IBC represents the cumulate in the typical LMO model by ref. 61. The IBC (this study) composition is the average value of the seven precursor rocks. The pressure setting of 3 kbar corresponds to the depth of IBC (~60–80 km) in the previous study[61]. The white dashed lines represent the contour lines of melt volume proportion in the system.

melting and sustain larger or longer-lived magma reservoirs. In this case, heterogeneity in the nearside IBC have a significant influence on the onset, extent and spatial distribution of partial melting, and consequently on the formation and localization of magma source regions.

The origin of the observed lunar nearside and farside mare asymmetry is a major unresolved problem in lunar science[69]. A series of remote sensing data suggests comparable age distributions[5,6,70] of nearside and farside mare volcanism, but a 20 times volume difference[71] between these two hemispheres. This dichotomy might be explained by the thinner crust of the nearside than the farside[8,9]. However, even in some farside regions with similar or thinner crustal thickness than that on the nearside[10,67,71] (e.g., the SPA basin), the volume of basalt did not significantly increase, indicating that crustal thickness is not the only factor controlling the distribution of mare basalt. The mechanism driven by radioactive heating[13,16] or melting point decrease[72] caused by deep heterogeneous KREEP is also difficult to play a role in the difference of young magmatism between nearside and farside, as it has not been confirmed in young basalts such as Chang'e-5 basalts[20] and Chang'e-6 basalts[26]. Especially, both Chang'e-5 (~2.0 Ga[18,19]) and Chang'e-6 basalts (~2.8 Ga[23,24]) are young mare basalts that exhibit similarly depleted isotopic characteristics[20,26], indicating a lack of KREEP contribution to their mantle sources. However, despite these compositional similarities, the magma volumes and eruption scales of the two differ markedly between the nearside and farside. This contrast suggests that the heterogeneous distribution of KREEP components did not exert a dominant influence on the asymmetry of late-stage lunar magmatism.

Alternatively, the asymmetry dominated by heterogeneity of other reservoirs, such as IBC, is possible, but the specific mechanism still needs further clarification[27,28]. Our study suggests that the IBC beneath the PKT in the nearside may contain ilmenite abundances significantly higher than average, leading to an increase in the degree of partial melting (Fig. 5). In other words, the ilmenite abundance in the farside IBC may correspondingly decrease, further leading to a decrease in the magma production (Fig. 5). Based on lunar global TiO_2 distribution[30], most of the high-Ti basalts that require IBC to participate in the source region formation are distributed near the PKT, while lacking in the farside. Furthermore, Gravity data from the GRAIL mission indicate the lateral density variations within the lunar crust and upper mantle at a global scale, especially the higher density, Bouguer gravity anomaly and gravity gradient beneath the PKT[73,74]. Similarly, the high electrical conductivity beneath the PKT has also been reported, distinguishing it from other lunar terrains and suggesting a possible enrichment in Fe-bearing materials[75]. These observations are consistent with the existence of a predicted ilmenite-rich layer beneath the nearside PKT. In addition, the elevated ilmenite abundance on the nearside leads to an increase in the IBC density, thereby inducing stronger mantle overturning[76,77], which is conducive to the generation of large-scale volcanism. This difference suggests that the composition of the initial system on the nearside is richer in TiO_2 than on the farside, which possibly originated from either inherited asymmetry in the LMO crystallization processes[78] or dynamic redistribution of compositionally stratified layers through thermomechanical forcing during the South Pole-Aitken (SPA) basin-forming

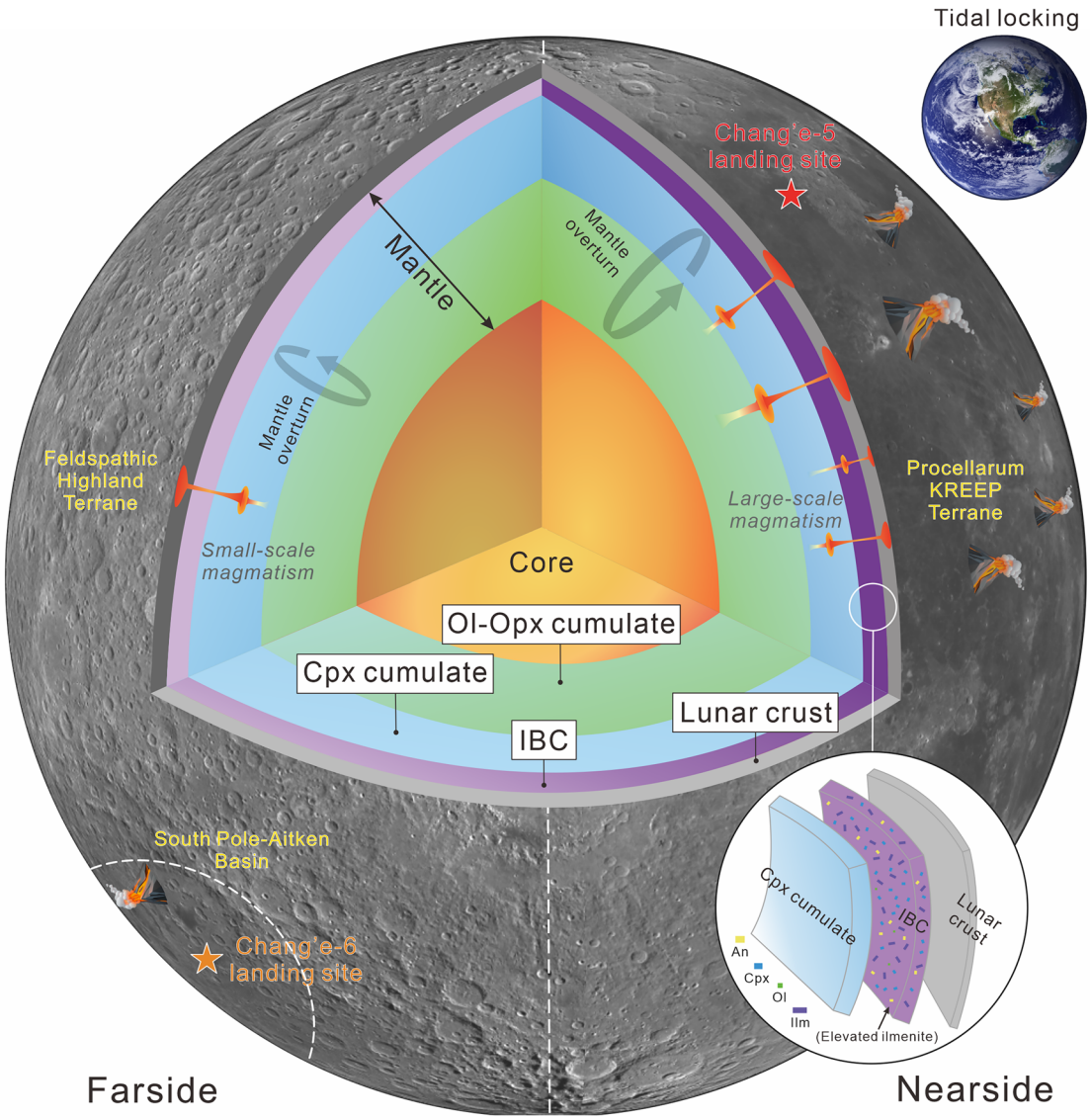

Fig. 5 | Schematic diagram of differential magmatism induced by IBC with different ilmenite abundance on the lunar nearside and farside. The diagram shows that the IBC beneath the PKT in the nearside may contain ilmenite abundances significantly higher than average, leading to an increase in the degree of partial melting and large-scale magmatism. This schematic diagram is not drawn to actual scale to highlight the IBC element. The darker and lighter purple colors of the IBC layer indicate higher and lower ilmenite abundances on the nearside and farside, respectively. The detailed layer structure was modified based on the ref. 104. Ol olivine, Opx orthopyroxene, Cpx clinopyroxene. The remote sensing image is from lunarquickmap at https://quickmap.lroc.im-ldi.com/. The elements of the Earth and volcano are from Aigei.com (a public third-party material library).

impact event[29,79]. In either case, the differences in the ilmenite-rich cumulate on the two hemispheres have various effects and could cause distinctive volcanic evolutionary processes in each hemisphere, helping to account for the observed mare basalt asymmetry (Fig. 5). Further studies with detailed analysis of glass beads within existing Apollo, Luna and Chang'e-5 collections, particularly from targeted locations, is essential for advancing our understanding of lunar evolution.

Materials and methods

Scanning electron microscope observations for the Chang'e-5 regolith sample

The four high-Ti glass beads in this study were obtained from a powder sample (CE5C0600) allocated by China National Space Administration. These glass beads were hand-picked, mounted, polished and carbon-coated. Then, polished mounts and carbon-coated mounts were examined for back-scattered electron (BSE) imaging with the scanning electron microscope (SEM, QUANTA FEG 650) at the Key Laboratory of Orogenic Belts and Crustal Evolution, School of Earth and Space Sciences, Peking University, Beijing. All analyses were conducted under an accelerating voltage of 10 kV and a working distance of 9.4–9.9 mm.

Major element analysis

Major elements of homogeneous and clean areas of four glass beads were obtained using the JEOL JXA-8230 electron microprobe at the Key Laboratory of Tibetan Plateau Earth System, Environment and Resources, Institute of Tibetan Plateau Research, Chinese Academy of Sciences. All samples were polished to a smooth surface again before conducting the mapping and point analysis of the Ti element, and the measurement points were placed in a homogeneous and clean area inside the glass bead. We analyzed at least 17 points on each glass bead (Supplementary Data 1) and conducted mapping analysis of the Ti element to evaluate its heterogeneity. The operating conditions were as follows: a 25.0 kV accelerating voltage, a

20 nA beam current and a 1–5 μm beam size. Natural minerals and synthetic minerals were used as standards, and all data has undergone ZAF correction processing. The typical detection limits for most of the analytical elements were 0.01 to 0.03 wt%. The mapping was conducted at an accelerating voltage of 15 kV and a beam current of 100 nA in stage-scan mode. The mapping was collected with a step width of 0.20 μm in both X and Y directions, and a dwell time of 60 ms per pixel. A typical mapping consists of 425 × 400 points, corresponding to an area of ~85 × 80 μm.

Trace-element analysis

The trace-element abundances in glass beads were completed by Xi'an Zhaonian Mineral Testing Technology with instruments including Thermo Fisher iCAP RQ ICP-MS and the accompanying New Wave NWR 213 laser ablation system. The laser diameter is about 30 μm with a repetition rate of 10 Hz. The laser energy density is approximately 6.0 J·cm^{-2}. Helium was employed as the ablation gas to improve the transport efficiency of ablated aerosols. Before testing, NIST 610 is used to adjust the instrument to achieve optimal performance. LA-ICP-MS laser ablation sampling adopts a single-point ablation method. During the testing process, the laser beam is first blocked for 20 s to collect a blank background, and then the sample is continuously eroded and collected for 45 s. After stopping the ablation, the injection system is further purged for 20 s to clean. The single-point testing analysis time is 85 seconds. NIST 610, NIST 612, BCR-2G, and BIR-1G glasses were used for quality control monitoring, and the relative standard deviation (1σ) is less than 5–10% for measured trace elements. The offline processing of analytical data (including the selection of samples and blank signals, instrument sensitivity drift correction and element content calculation) is completed by software ICPMSData Cal. The calibration of trace elements was carried out using the average Si content obtained by EPMA as the internal standard.

Fractional crystallization modeling

The PETROLOG program[80] was employed to simulate forward fractional crystallization processes to reconstruct the evolutionary pathway of high-Ti basalts and cumulate production of Chang'e-5 lava. The source region composition of high-Ti basalt was based on the average composition of Apollo black glass beads (Supplementary Data 2). The simulation was based on pure fractional crystallization (100%) at a constant pressure. All Fe was treated as Fe^{2+} (FeO) and Fe_2O_3 content in the system was determined by the $Fe^{3+} = 0$. Mineral solution models include olivine[81], clinopyroxene[82], orthopyroxene[83], plagioclase[82], and ilmenite[84]. The pressure for near-surface fractionation was set at 1 kbar (~15 km depth), as pressures below 1 kbar yielded negligible differences in modeling results[27]. Specific simulation details of fractional crystallization follow ref. 27.

Phase-equilibrium modeling

Phase-equilibrium modeling was conducted by GeoPS program[85]. GeoPS provides a wide range of phase equilibria calculations and illustration facilities based on the Gibbs free energy minimization method. The applications include calculation of various types of phase diagrams, isopleths, and thermodynamic modeling for path-dependent open system processes. The modeling is based on the nine-component K_2O-Na_2O-CaO-FeO-MgO-Al_2O_3-SiO_2-TiO_2-Cr_2O_3 system and tc-ds634[86]. The calculation of the phase diagram in Fig. 3A uses the average composition of the high-Ti glass beads. The mineral modal abundance and compositions in Fig. 3B–D were calculated based on the composition of each sample by reducing the temperature below the solidus line under a pressure of 1 bar. This step restores the process that precursor rock was impacted to form glass beads on the lunar surface.

Mineral assemblage calculation in the LMO

Considering that quartz and a portion of anorthite float to form lunar crust[59], we restored the mineral modal abundance of LMO crystallization (that is, the mineral abundance before anorthite and quartz flotation). We assumed that the mineral abundance in the precursor rock of high-Ti glass beads represents the cumulate component after flotation. We calculated the mineral abundance of seven samples under different proportions of residual anorthite. Assuming that the residual anorthite represents 0.01-0.4 of the total anorthite, we added a varying amount of anorthite back into the precursor rock based on the ratio between residual and residual + flotation anorthite, then calculated the modal proportion of each phase relative to the new total. The minerals before flotation include clinopyroxene, ilmenite, anorthite, olivine and quartz, while residual minerals after flotation include clinopyroxene, ilmenite, anorthite, olivine (Fig. 3A). Although the quartz proportion is unknown, it is roughly similar in different LMO models, so 11.5 vol% quartz[61] is used for calculation.

REE modeling

Based on the observed REE results, we conducted a mixed REE modeling for high-Ti glass beads to explore their formation process. In fact, the observed REE abundances of high-Ti glass beads in this study are significantly higher than those of normal IBC obtained from thermodynamic calculations[59]. However, the numerical simulation results indicate that the efficiency of IBC sinking into the deep part is low during the mantle overturn, and a certain proportion of IBC was retained in the shallow part and mixed with the KREEP layer[87]. Therefore, we conducted a mixed REE modeling using IBC (90–95 PCS) and high-K KREEP components. The compositions of 90–95 PCS and high-K KREEP were collected from refs. 59,88, respectively. The modeling results show that the addition of 10–50% KREEP components into 95 PCS can match the observed REE patterns (Supplementary Fig. 5).

Data availability

All data in this study could be found at https://doi.org/10.6084/m9.figshare.31144267.v1. The analytical data and detailed results of fractional crystallization and phase equilibrium modeling are available in the Supplementary Materials. The PETROLOG program and GeoPS program are available at https://petrologsoftware.com/ and http://www.geology.ren/zh-cn/index.html. We acknowledge the use of imagery from Lunar QuickMap (https://quickmap.lroc.im-ldi.com/), a collaboration in the public domain between NASA, Arizona State University & Applied Coherent Technology Corp. Some materials in the schematic diagram are sourced from https://www.aigei.com, and the material is licensed for use under the CCE0 protocol (https://www.aigei.com/about/copyright).

Received: 6 August 2025; Accepted: 4 February 2026;
Published online: 14 February 2026

References

1. Wieczorek, M. A. et al. The crust of the moon as seen by GRAIL. *Science* **339**, 671–675 (2012).
2. Smith, D. E. et al. Initial observations from the Lunar Orbiter Laser Altimeter (LOLA). *Geophys. Res. Lett.* **37**, L18204 (2010).
3. Nelson, D. M. et al. Mapping Lunar Maria Extents and Lobate Scarps Using LROC Image Products. In *45th Annual Lunar and Planetary Science Conference* edited 2861, (The Woodlands, Texas, 2014).
4. Hiesinger, H. et al. The lunar cratering chronology. *Rev. Mineral. Geochem.* **89**, 401–451 (2023).
5. Head, J. W. et al. Lunar mare basaltic volcanism: volcanic features and emplacement processes. *Rev. Mineral. Geochem.* **89**, 453–507 (2023).
6. Qian, Y. et al. Long-lasting farside volcanism in the Apollo basin: Chang'e-6 landing site. *Earth Planet. Sci. Lett.* **637**, 118737 (2024).
7. Pasckert, J. H., Hiesinger, H. & van der Bogert, C. H. Lunar farside volcanism in and around the South Pole–Aitken basin. *Icarus* **299**, 538–562 (2018).
8. Solomon, S. Mare volcanism and lunar crustal structure. *Proc. Lunar Sci. Conf.* **6th**, 1021–1042 (1975).
9. Head, J. W. & Wilson, L. Lunar mare volcanism: stratigraphy, eruption conditions, and the evolution of secondary crusts. *Geochim. Cosmochim. Acta* **56**, 2155–2175 (1992).

10. Head, J. W. & Wilson, L. Generation, ascent and eruption of magma on the Moon: new insights into source depths, magma supply, intrusions and effusive/explosive eruptions (Part 2: predicted emplacement processes and observations). *Icarus* **283**, 176–223 (2017).
11. Ishihara, Y. et al. Crustal thickness of the Moon: Implications for farside basin structures. *Geophys. Res. Lett.* **36**, L19202 (2009).
12. Head, J. W., Wang, X., Lark, L. H., Wilson, L. & Qian, Y. Lunar nearside-farside mare basalt asymmetry: the combined role of global crustal thickness variations and South Pole-Aitken (SPA) basin-induced lithospheric thickening. *Geophys. Res. Lett.* **51**, e2024GL110510 (2024).
13. Borg, L. E., Shearer, C. K., Asmerom, Y. & Papike, J. J. Prolonged KREEP magmatism on the Moon indicated by the youngest dated lunar igneous rock. *Nature* **432**, 209–211 (2004).
14. Meyer, C. et al. Mineralogy, chemistry, and origin of the KREEP component in soil samples from the Ocean of Storms. In *Proc. 2nd Lunar Science Conference* 393–411 (MIT Press, 1971).
15. Laneuville, M., Taylor, J. & Wieczorek, M. A. Distribution of radioactive heat sources and thermal history of the Moon. *J. Geophys. Res.* **123**, 3144–3166 (2018).
16. Warren, P. H. The magma ocean concept and lunar evolution. *Annu. Rev. Earth Planet. Sci.* **13**, 201–240 (1985).
17. Elkins-Tanton, L. T., Burgess, S. & Yin, Q.-Z. The lunar magma ocean: Reconciling the solidification process with lunar petrology and geochronology. *Earth Planet. Sci. Lett.* **304**, 326–336 (2011).
18. Che, X. et al. Age and composition of young basalts on the Moon, measured from samples returned by Chang'e-5. *Science* **374**, 887–890 (2021).
19. Li, Q.-L. et al. Two-billion-year-old volcanism on the Moon from Chang'e-5 basalts. *Nature* **600**, 54–58 (2021).
20. Tian, H.-C. et al. Non-KREEP origin for Chang'e-5 basalts in the Procellarum KREEP Terrane. *Nature* **600**, 59–63 (2021).
21. Zong, K. et al. Bulk compositions of the Chang'E-5 lunar soil: Insights into chemical homogeneity, exotic addition, and origin of landing site basalts. *Geochim. Cosmochim. Acta* **335**, 284–296 (2022).
22. Elardo, S. M. et al. A shallow mantle source for the Chang'e 5 lavas reveals how top-down heating prolonged lunar magmatism. *Sci. Adv.* **11**, eadr1486 (2025).
23. Zhang, Q. W. L. et al. Lunar farside volcanism 2.8 billion years ago from Chang'e-6 basalts. *Nature* **643**, 356–360 (2025).
24. Cui, Z. X. et al. A sample of the Moon's far side retrieved by Chang'e-6 contains 2.83-billion-year-old basalt. *Science* **386**, 1395–1399 (2024).
25. Che, X. C. et al. Isotopic and compositional constraints on the source of basalt collected from the lunar farside. *Science* **387**, 1306–1310 (2025).
26. Zhou, Q. et al. Ultra-depleted mantle source of basalts from the South Pole–Aitken basin. *Nature* **643**, 371–375 (2025).
27. Su, B. et al. Fusible mantle cumulates trigger young mare volcanism on the cooling Moon. *Sci. Adv.* **8**, eabn2103 (2022).
28. Wang, C. et al. A shallow (<100 km) ilmenite-bearing pyroxenitic source for young lunar volcanism. *Earth Planet. Sci. Lett.* **639**, 118770 (2024).
29. Zhang, N. et al. Lunar compositional asymmetry explained by mantle overturn following the South Pole–Aitken impact. *Nat. Geosci.* **15**, 37–41 (2022).
30. Sato, H. et al. Lunar mare TiO2 abundances estimated from UV/Vis reflectance. *Icarus* **296**, 216–238 (2017).
31. Kato, S. et al. Magma source transition of lunar mare volcanism at 2.3 Ga. *Meteorit. Planet. Sci.* **52**, 1899–1915 (2017).
32. Li, C. et al. Characteristics of the lunar samples returned by the Chang'E-5 mission. *Natl. Sci. Rev.* **9**, nwab188 (2021).
33. Jolliff, B. L., Gillis, J. J., Haskin, L. A., Korotev, R. L. & Wieczorek, M. A. Major lunar crustal terranes: surface expressions and crust-mantle origins. *J. Geophys. Res.* **105**, 4197–4216 (2000).
34. Zeng, X., Li, X. & Liu, J. Exotic clasts in Chang'e-5 regolith indicative of unexplored terrane on the Moon. *Nat. Astron.* **7**, 152–159 (2023).
35. Qian, Y. et al. Copernican-aged (<200 Ma) impact ejecta at the Chang'e-5 landing site: statistical evidence from crater morphology, morphometry, and degradation models. *Geophys. Res. Lett.* **48**, e2021GL095341 (2021).
36. Sheng, S.-Z. et al. Orthopyroxene-dominated upper mantle melting built the early crust of the Moon. *Commun. Earth Environ.* **5**, 403 (2024).
37. Ding, C.-L. et al. A potential mantle origin for precursor rocks of high-Mg impact glass beads in Chang'e-5 soil. *Sci. Adv.* **11**, eadv9019 (2025).
38. Keller, L. P. & McKay, D. S. Discovery of vapor deposits in the lunar regolith. *Science* **261**, 1305–1307 (1993).
39. Pieters, C. M. & Noble, S. K. Space weathering on airless bodies. *J. Geophys. Res.* **121**, 1865–1884 (2016).
40. Yan, P. et al. Intricate regolith reworking processes revealed by microstructures on lunar impact glasses. *J. Geophys. Res.* **127**, e2022JE007260 (2022).
41. Yan, P., Xiao, Z., Wu, Y., Pan, Q. & Wu, Y. Iron-rich grain-decorated depressions on surfaces of lunar impact glasses. *J. Geophys. Res.* **129**, e2024JE008284 (2024).
42. Long, T. et al. Constraining the formation and transport of lunar impact glasses using the ages and chemical compositions of Chang'e-5 glass beads. *Sci. Adv.* **8**, eabq2542 (2022).
43. Yang, W. et al. Geochemistry of impact glasses in the Chang'e-5 regolith: constraints on impact melting and the petrogenesis of local basalt. *Geochim. Cosmochim. Acta* **335**, 183–196 (2022).
44. Wang, B.-W. et al. Returned samples indicate volcanism on the Moon 120 million years ago. *Science* **385**, 1077–1080 (2024).
45. Delano, J. W. Pristine lunar glasses: criteria, data, and implications. *J. Geophys. Res.* **91**, 201–213 (1986).
46. Nemchin, A. A., Whitehouse, M. J., Grange, M. L. & Muhling, J. R. On the elusive isotopic composition of lunar Pb. *Geochim. Cosmochim. Acta* **75**, 2940–2964 (2011).
47. Shearer, C. K. & Papike, J. J. Basaltic magmatism on the Moon: a perspective from volcanic picritic glass beads. *Geochim. Cosmochim. Acta* **57**, 4785–4812 (1993).
48. Zeigler, R. A., Korotev, R. L., Jolliff, B. L., Haskin, L. A. & Floss, C. The geochemistry and provenance of Apollo 16 mafic glasses. *Geochim. Cosmochim. Acta* **70**, 6050–6067 (2006).
49. Head, J. W. & Wilson, L. Rethinking lunar mare basalt regolith formation: new concepts of lava flow protolith and evolution of regolith thickness and internal structure. *Geophys. Res. Lett.* **47**, e2020GL088334 (2020).
50. Qian, Y. et al. The regolith properties of the Chang'e-5 landing region and the ground drilling experiments using lunar regolith simulants. *Icarus* **337**, 113508 (2020).
51. Li, Z. et al. Structures, compositions, and origins of glass beads in the lunar Chang'e-5 samples reveal the complexity of local regolith. *GSA Bull.* **138**, 654–672 (2025).
52. Wang, B.-W. et al. Size matters: chemical representativeness of lunar impact-generated glass beads. *Atom. Spectrosc.* **46**, 119–130 (2025).
53. Qian, Y. et al. China's Chang'e-5 landing site: geology, stratigraphy, and provenance of materials. *Earth Planet. Sci. Lett.* **561**, 116855 (2021).
54. Singletary, S. & Grove, T. Origin of lunar high-titanium ultramafic glasses: a hybridized source? *Earth Planet. Sci. Lett.* **268**, 182189 (2008).

55. Mallik, A., Ejaz, T., Shcheka, S. & Garapic, G. A petrologic study on the effect of mantle overturn: implications for evolution of the lunar interior. *Geochim. Cosmochim. Acta* **250**, 238–250 (2019).
56. Haupt, C. P., Renggli, C. J., Rohrbach, A., Berndt, J. & Klemme, S. Experimental constraints on the origin of the lunar high-Ti basalts. *J. Geophys. Res.* **129**, e2023JE008239 (2024).
57. Münker, C. A high field strength element perspective on early lunar differentiation. *Geochim. Cosmochim. Acta* **74**, 7340–7361 (2010).
58. Shepherd, K., Namur, O., Toplis, M. J., Devidal, J.-L. & Charlier, B. Trace element partitioning between clinopyroxene, magnetite, ilmenite and ferrobasaltic to dacitic magmas: an experimental study on the role of oxygen fugacity and melt composition. *Contrib. Mineral. Petrol.* **177**, 90 (2022).
59. Snyder, G. A., Taylor, L. A. & Neal, C. R. A chemical model for generating the sources of mare basalts: Combined equilibrium and fractional crystallization of the lunar magmasphere. *Geochim. Cosmochim. Acta* **56**, 3809–3823 (1992).
60. Longhi, J. Petrogenesis of picritic mare magmas: constraints on the extent of early lunar differentiation. *Geochim. Cosmochim. Acta* **70**, 5919–5934 (2006).
61. Lin, Y., Tronche, E. J., Steenstra, E. S. & van Westrenen, W. Experimental constraints on the solidification of a nominally dry lunar magma ocean. *Earth Planet. Sci. Lett.* **471**, 104–116 (2017).
62. Rapp, J. F. & Draper, D. S. Fractional crystallization of the lunar magma ocean: updating the dominant paradigm. *Meteorit. Planet. Sci.* **53**, 1432–1455 (2018).
63. Qian, Y. et al. Young lunar mare basalts in the Chang'e-5 sample return region, northern Oceanus Procellarum. *Earth Planet. Sci. Lett.* **555**, 116702 (2021).
64. Xie, M., Xiao, Z., Zhang, X. & Xu, A. The provenance of regolith at the Chang'e-5 candidate landing region. *J. Geophys. Res* **125**, e2019JE006112 (2020).
65. Miljković, K. et al. Excavation of the lunar mantle by basin-forming impact events on the Moon. *Earth Planet. Sci. Lett.* **409**, 243–251 (2015).
66. Moriarty III, D. P., Dygert, N., Valencia, S. N., Watkins, R. N. & Petro, N. E. The search for lunar mantle rocks exposed on the surface of the Moon. *Nat. Commun.* **12**, 4659 (2021).
67. Charlier, B., Grove, T. L., Namur, O. & Holtz, F. Crystallization of the lunar magma ocean and the primordial mantle-crust differentiation of the Moon. *Geochim. Cosmochim. Acta* **234**, 50–69 (2018).
68. Van Orman, J. & Grove, T. L. Origin of lunar high-titanium ultramafic glasses: constraints from phase relations and dissolution kinetics of clinopyroxene-ilmenite cumulates. *Meteoritics* **35**, 783–794 (2000).
69. Kring, D. A. & Durda, D. D. *A Global Lunar Landing Site Study to Provide the Scientific Context for Exploration of the Moon* (Lunar and Planetary Institute, 2012).
70. Haruyama, J. et al. Long-lived volcanism on the lunar farside revealed by SELENE Terrain Camera. *Science* **323**, 905–908 (2009).
71. Taguchi, M., Morota, T. & Kato, S. Lateral heterogeneity of lunar volcanic activity according to volumes of mare basalts in the farside basins. *J. Geophys. Res.* **122**, 1505–1521 (2017).
72. Elardo, S. M. et al. Early crust building enhanced on the Moon's nearside by mantle melting-point depression. *Nat. Geosci.* **13**, 339–343 (2020).
73. Besserer, J. et al. GRAIL gravity constraints on the vertical and lateral density structure of the lunar crust. *Geophys. Res. Lett.* **41**, 5771–5777 (2014).
74. Andrews-Hanna, J. et al. Structure and evolution of the lunar Procellarum region as revealed by GRAIL gravity data. *Nature* **514**, 68–71 (2014).
75. Grimm, R. E. Geophysical constraints on the lunar Procellarum KREEP Terrane. *J. Geophys. Res.* **118**, 768–777 (2013).
76. Tokle, L., Hirth, G., Liang, Y., Raterron, P. & Dygert, N. The effect of pressure and Mg-content on ilmenite rheology: implications for lunar cumulate mantle overturn. *J. Geophys. Res.* **126**, e2020JE006494 (2021).
77. Li, H. et al. Lunar cumulate mantle overturn: a model constrained by ilmenite rheology. *J. Geophys. Res.* **124**, 1357–1378 (2019).
78. Ohtake, M. et al. Asymmetric crustal growth on the Moon indicated by primitive farside highland materials. *Nat. Geosci.* **5**, 384–388 (2012).
79. Jones, M. J. et al. A South Pole-Aitken impact origin of the lunar compositional asymmetry. *Sci. Adv.* **8**, eabm8475 (2022).
80. Danyushevsky, L. V. & Plechov, P. Petrolog3: integrated software for modeling crystallization processes. *Geochem. Geophys. Geosyst.* **12**, Q07021 (2011).
81. Ford, C. E., Russell, D. G., Groven, J. A. & Fisk, M. R. Olivine-liquid equilibria: temperature, pressure and composition dependence of the crystal/liquid cation partition coefficients for Mg, Fe^{2+}, Ca, Mn. *J. Petrol.* **24**, 256–266 (1983).
82. Danyushevsky, L. V. The effect of small amounts of H2O on crystallisation of mid-ocean ridge and backarc basin magmas. *J. Volcanol. Geotherm. Res.* **110**, 265–280 (2001).
83. Beattie, P. Olivine–melt and orthopyroxene–melt equilibria. *Contrib. Mineral. Petrol.* **115**, 103–111 (1993).
84. Nielsen, R. L. EQUIL: a program for the modeling of low-pressure differentiation processes in natural mafic magma bodies. *Comput. Geosci.* **11**, 531–546 (1985).
85. Xiang, H. & Connolly, J. A. D. GeoPS: an interactive visual computing tool for thermodynamic modelling of phase equilibria. *J. Metamorph. Geol.* **40**, 243–255 (2022).
86. Holland, T. J. B. & Powell, R. An improved and extended internally consistent thermodynamic dataset for phases of petrological interest, involving a new equation of state for solids. *J. Metamorph. Geol.* **29**, 333–383 (2011).
87. Zhao, Y., de Vries, J., van den Berg, A. P., Jacobs, M. H. G. & van Westrenen, W. The participation of ilmenite-bearing cumulates in lunar mantle overturn. *Earth Planet. Sci. Lett.* **511**, 1–11 (2019).
88. Warren, P. H. *Moon in Transition: Apollo 14, KREEP, and Evolved Lunar Rocks*. Report No. 89-03 (Lunar and Planetary Institute, 1989).
89. Saal, A. E. et al. Volatile content of lunar volcanic glasses and the presence of water in the Moon's interior. *Nature* **454**, 192–195 (2008).
90. Saal, A. E. & Hauri, E. H. Large sulfur isotope fractionation in lunar volcanic glasses reveals the magmatic differentiation and degassing of the Moon. *Sci. Adv.* **7**, eabe4641 (2021).
91. Chao, E. C. T., Boreman, J. A., Minkin, J. A., James, O. B. & Desborough, G. A. Lunar glasses of impact origin: Physical and chemical characteristics and geologic implications. *J. Geophys. Res.* **75**, 7445–7479 (1970).
92. Glass, B. P. Investigation of glass recovered from Apollo 12 sample 12057. *J. Geophys. Res.* **76**, 5649–5657 (1971).
93. Meyer Jr. C. et al. Mineralogy, chemistry, and origin of the KREEP component in soil samples from the Ocean of Storms. In *Proc. Second Lunar Science Conference* 393–411 (MIT Press, 1971).
94. Delano, J. W., Lindsley, D. & Rudowski, R. Glasses of impact origin from Apollo 11, 12, 15, and 16:evidence for fractional vaporization and mare/highland mixing. In *Proc. 12th Lunar and Planetary Science Conference* 339–370 (Pergamon Press, 1981).
95. Wentworth, S. J. et al. Apollo 12 ropy glasses revisited. *Meteoritics* **29**, 323–333 (1994).
96. Zellner, N. E. B., Spudis, P. D., Delano, J. W. & Whittet, D. C. B. Impact glasses from the Apollo 14 landing site and implications for regional geology. *J. Geophys. Res. Planets* **107**, 5102 (2002).
97. Zellner, N. E. B. et al. Evidence from $^{40}Ar/^{39}Ar$ ages of lunar impact glasses for an increase in the impact rate 800 Ma ago. *Geochim. Cosmochim. Acta* **73**, 4590–4597 (2009).

98. Zellner, N. E. B. & Delano, J. W. $^{40}Ar/^{39}Ar$ ages of lunar impact glasses: relationships among Ar diffusivity, chemical composition, shape, and size. *Geochim. Cosmochim. Acta* **161**, 203–218 (2015).
99. Nguyen, P. & Zellner, N. Using size and composition to assess the quality of lunar impact glass ages. *Geoscience* **9**, 85 (2019).
100. Nemchin, A. A. et al. U-Pb isotope systematics and impact ages recorded by a chemically diverse population of glasses from an Apollo 14 lunar soil. *Geochim. Cosmochim. Acta* **321**, 206–243 (2022).
101. He, Q. et al. Detailed petrogenesis of the unsampled Oceanus Procellarum: the case of the Chang'e-5 mare basalts. *Icarus* **383**, 115082 (2022).
102. Jiang, Y. et al. Fe and Mg isotope compositions indicate a hybrid mantle source for young Chang'E 5 mare basalts. *Astrophys. J. Lett.* **945**, L26 (2023).
103. McDonough, W. F. & Sun, S. S. The composition of the Earth. *Chem. Geol.* **120**, 223–253 (1995).
104. Ju, D., Pang, R., Rui, L. I. & Du, W. The initial lunar mantle structure constrained by thermodynamic simulation. *Acta Petrol. Sin.* **38**, 1025–1042 (2022).
105. Takazawa, E., Frey, F. A., Shimizu, N. & Obata, M. Whole rock compositional variations in an upper mantle peridotite (Horoman, Hokkaido, Japan): are they consistent with a partial melting process?. *Geochim. Cosmochim. Acta* **64**, 695–716 (2000).
106. Davis, F. A., Tangeman, J. A., Tenner, T. J. & Hirschmann, M. M. The composition of KLB-1 peridotite. *Am. Mineral.* **94**, 176–180 (2009).
107. Ringwood, A. E. *Origin of the Earth and Moon* (Springer-Verlag, 1979).
108. Hauri, E. H., Saal, A. E., Rutherford, M. J. & Van Orman, J. A. Water in the Moon's interior: truth and consequences. *Earth Planet. Sci. Lett.* **409**, 252–264 (2015).
109. Taylor, S. R. *Planetary Science: A Lunar Perspective* (Lunar and Planetary Institute, 1982).

Acknowledgements

We are grateful to the China National Space Administration (CNSA) for providing the Chang'e-5 samples. Thanks for the insightful comments from Professor Alexander Nemchin, which help to improve the manuscript quality. We are grateful to Editor Prof. Brittany Cymes, Deputy Editor Joe Aslin, reviewer Christopher Yen and reviewer Cordula Haupt for their constructive comments on our manuscript. This study was supported by the National Natural Science Foundation of China (No. 42241107). YQ was funded by the HK RGC GRF 17307025, JLFS/P-702/24, and the Seed Fund for Basic Research for New Staff (2401102770).

Author contributions

Conceptualization: Z.L. and Y.Q. Methodology: Z.L. and B.Z. Investigation: Z.L., T.L., and X.C. Visualization: Y.Q. and J.W.H. Supervision: B.Z. Writing—original draft: Z.L. and B.Z. Writing—review & editing: Y.Q. and J.H.

Competing interests

The authors declare no competing interests.

Additional information

Supplementary information The online version contains supplementary material available at https://doi.org/10.1038/s43247-026-03300-w.

Correspondence and requests for materials should be addressed to Bo Zhang or Yuqi Qian.

Peer review information *Communications Earth & Environment* thanks Cordula Haupt and Christopher Yen for their contribution to the peer review of this work. Primary Handling Editors: Brittany Cymes, Joe Aslin and Carolina Ortiz Guerrero. A peer review file is available.